Flux pinning force in bulk MgB_2 with variable grain size

E. Martínez,[1,*] P. Mikheenko,[2,†] M. Martínez-López,[1] A. Millán,[1] A. Bevan,[2] and J. S. Abell[2]
[1]*Instituto de Ciencia de Materiales de Aragón, CSIC–Universidad de Zaragoza, C/María de Luna 3, 50018 Zaragoza, Spain*
[2]*Metallurgy and Materials, School of Engineering, University of Birmingham, Edgbaston, Birmingham B15 2TT, United Kingdom*
(Received 31 October 2006; revised manuscript received 21 December 2006; published 20 April 2007)

We report temperature and magnetic-field dependence of flux pinning force in bulk MgB_2 with variable grain size. The samples are prepared by advanced methods, allowing minimizing effects of porosity, impurities, and inclusions of secondary phases. The effects of grain connectivity, flux-creep phenomena, and grain size on critical current density and flux pinning curves are analyzed. We have compared the field dependence of the pinning force for a range of samples with the predictions of theoretical models accounting for the effect of the grain size. There is qualitative agreement between grain-boundary pinning mechanism proposed by Hampshire and Jones [J. Phys. C **21**, 419 (1987)] and the experimentally observed grain-size dependence of pinning force in bulk MgB_2.

DOI: 10.1103/PhysRevB.75.134515 PACS number(s): 74.25.Qt, 74.70.Ad, 74.25.Ha, 74.25.Sv

I. INTRODUCTION

The MgB_2 superconductor[1] reveals very high potential for use in electric power applications and electronic devices. Unlike conventional low-temperature superconductors (LTSs) such as Nb-Ti and Nb_3Sn, the high critical temperature of MgB_2, $T_c \sim 39$ K, allows its operation in liquid hydrogen (20 K) or at temperatures between 20 and 30 K easily reachable with cryocoolers. A disadvantage of MgB_2 is its relatively low irreversibility field, B_{irr}. Therefore, special efforts are undertaken to clarify how to improve the superconducting properties of MgB_2, particularly the critical current density J_c, in high magnetic fields. Up to now, the highest J_c values at temperatures of 5–20 K in magnetic fields above 3 T have been achieved by doping with SiC nanoparticles;[2] but other factors, such as the decrease of grain size, are also effective in increasing J_c at high fields.[3] The poor electrical connectivity between grains, porosity, and the presence of secondary phases are among the main restricting factors for J_c, even in low fields, and their influence can easily exceed the benefits of having effective pinning centers in high fields.

Flux pinning force densities, $F_p = -J_c \times B$, can be useful in analyzing the mechanisms that control J_c in these materials. The pinning force of superconductors is a function of temperature and magnetic field and is determined by the micro- and nanostructure of the sample. Fietz and Webb[4] observed that the temperature and field dependence of F_p follow a scaling law of the form $F_p = CB_{c2}^m b^p (1-b)^q$, where $b = B/B_{c2}$ is the reduced induction, B_{c2} is the upper critical field, and C is a constant, which depends on the microstructure and intrinsic properties of the specimen. This $F_p(b)$ has a maximum at $b_{peak} = p/(p+q)$. The field dependence of the normalized flux pinning force gives an indication of the pinning mechanisms operative in a particular case.[5] For many practical superconductors, both high-temperature superconductor and LTS, J_c may become zero at magnetic fields lower than B_{c2} and, therefore, the field $B^* = B(J_c \to 0)$ is used instead of B_{c2} to scale the F_p curves. In order to analyze the pinning properties of MgB_2 superconductors, it is also essential to study the effect of flux creep on the F_p curves. High flux-creep rates, which would impose serious limitations to many technological applications, would also result in strong time dependent $F_p(b)$ curves.

In this paper, we describe the pinning properties of bulk MgB_2 samples prepared by different methods: hot isostatic pressing (HIP), resistive sintering (RS), and powder-in-tube (PIT) technique. The samples with different microstructure and superconducting properties have been obtained using different precursors and processing conditions. We discuss the role of the extrinsic characteristics, such as grain size and grain connectivity, and intrinsic properties, such as the Ginzburg-Landau parameter κ and flux-creep effects, on the flux pinning force in MgB_2. A comparison between the experimental results and predictions of theoretical models will be given.

II. EXPERIMENT

The main parameters of the analyzed MgB_2 samples are shown in Table I. The bulk samples were prepared by three different methods: HIP, RS, and PIT. In HIP, a precompacted powder was enclosed in a steel container, evacuated, and pressed in a high-pressure (1 kbar) argon atmosphere at temperatures of 940–1000 °C for 4–12 h. Resistive sintering was performed in a high-pressure graphite die with tungsten rods that created a uniaxial pressure and simultaneously acted as electrodes to carry high electrical currents, about 500 A. The inner diameter of the die used was 5 mm and the applied pressure was 550 bar. The densification of powder took place in vacuum with a remnant pressure below 10^{-4} Torr. The electrical current heated the sample up to 900 °C. The SiC-doped sample (B-SiC) was prepared from mechanically alloyed powders of composition $MgB_{1.9}(SiC)_{0.1}$. The average grain size of the SiC nanoparticles was 30 nm.

The PIT composite nickel-sheathed wires were prepared as described in Ref. 6. The initial powders were prereacted MgB_2 and $MgB_{1.8}(SiC)_{0.1}$, which had been previously obtained from the elements Mg, B, and nano-SiC (average grain size of 30 nm). These powders were vacuum sealed in a quartz tube and treated at 640 °C for 0.5 h and then at 850 °C for 1 h. Subsequently, the powders were packed in-

 ©2007 The American Physical Society

TABLE I. Processing parameters, dimensions of the bulk samples used for magnetic measurements, and resistivity values of the analyzed MgB_2 samples, $\Delta\rho=\rho(300\ \mathrm{K})-\rho(40\ \mathrm{K})$. The grain size D corresponds to the average value estimated by EBSD.

Sample ID		Processing method	D (nm)	Dimensions (values in mm)	$\rho(40\ \mathrm{K})$ ($\mu\Omega$ cm)	$\rho(300\ \mathrm{K})$ ($\mu\Omega$ cm)	$\Delta\rho$ ($\mu\Omega$ cm)	RRR $=\rho(300\ \mathrm{K})/\rho(40\ \mathrm{K})$
B1	Undoped	HIP	80	$4.6\times1.25\times1.2$	6.6	18	11.4	2.7
B2	Undoped	RS	95	$4.85\times0.9\times0.7$				
B3	Undoped	HIP	400	$4.7\times2.45\times0.85$	4.4	13	8.6	3.0
B4	Undoped	HIP	2200	$3.55\times1.35\times0.85$	22	57	35	2.6
B5	Undoped	HIP	160	$4.2\times1.95\times0.9$	26	78	52	3.0
B-SiC	SiC-doped	HIP	60	$4.75\times1.8\times0.8$	27	42	15	1.6

side 4 mm diam Ni tubes, which was cold drawn down to 1.15 mm diam, having typical core diameters of 0.60–0.65 mm. The in-wire reaction was done in sealed quartz tubes with argon at 850 °C for 0.5 h. Because of Ni ferromagnetism, to perform the magnetic measurements the sheath was removed by polishing without any apparent deterioration of the superconducting properties. The measured PIT samples, both undoped (W) and SiC doped (W-SiC), were of the length $L=4.5$ mm and diameter $\phi=0.6$ mm.

The magnetic measurements were carried out using a superconducting quantum interference device (Quantum Design MPMS 5T) and a vibrating sample magnetometer (Quantum Design PPMS 9T). The field was applied parallel to the longest dimension of the samples. The resistivity measurements $\rho(T)$ have also been carried out using the Quantum Design PPMS system on 1-cm-long samples obtained from the same batch. The values of ρ at $T=40$ K and the residual resistivity ratio, $\mathrm{RRR}=\rho(300\ \mathrm{K})/\rho(40\ \mathrm{K})$, for some of the analyzed samples are shown in Table I. These measurements could not be made in all samples due to the small length of some of them.

We used electron backscatter diffraction (EBSD) and transmission electron microscopy (TEM) to clarify the micro- and nanostructure of the samples. EBSD is an advanced method that maps crystallinity of the samples. This technique allows quantification of grain size, orientations, misorientations, textures, and properties of the grain boundaries on micro- and nanoscale. EBSD is available in state-of-the-art scanning electron microscopes (SEM). In this work, we used SEM JEOL7000. EBSD is a surface technique with data being acquired from a depth of tens of nanometers. TEM observations on crushed samples were carried out with a Jeol 2000 FXII microscope.

III. RESULTS AND DISCUSSION

A. Microstructure

We performed detailed EBSD analyses to estimate the grain-size distribution of all measured RS and HIP samples. A TEM investigation of selective samples to confirm the features found in EBSD has also been performed. Figures 1(a) and 1(b) show a SEM image of sample B3 and its corresponding EBSD map, respectively. The porosity varies between 7% to 15% in all analyzed HIP and RS bulk samples. The grains are single crystals as identified by a single color (gray scale) in Fig. 1(b). Different colors (gray scales) represent different orientations of the crystal lattice in the grains. Black shows unsolved areas. The EBSD images have some noise, mostly in the form of isolated pixels. Therefore, we have removed these pixels, as shown in Fig. 1(c), to calculate the grain-size distribution [Fig. 1(d)], where D is the equivalent diameter defined as $D=2(A/\pi)^{1/2}$ and A is the area of a grain. The average grain size in this sample, estimated from several EBSD images, is 400 nm. Although, as shown in Fig. 1(d), grains as large as 2 μm are present in the sample, the majority of the grains have D about 200 nm (abrupt peak in the histogram). The average grain sizes for the different samples are collected in Table I. Samples B1, B2, B4, and B-SiC have narrow grain distributions. Sample B5 has an average grain size of 160 nm, with most grains in the range of 80–90 nm and some bigger grains of a few microns. The error in the estimation of grain size mainly relates to the EBSD resolution, about 50 nm. Moreover, since the number of pixels of the EBSD images is fixed, the pixel size depends on the used scale. The EBSD technique also allows the analysis of misorientation between neighbor grains. The analysis made in these RS and HIP samples shows that misorientation angles are almost random for most samples, with slight variations in the angle distribution among the different samples. Figure 2 shows a TEM image of sample B3 whose EBSD maps are shown in Fig. 1. The large grains of the order of microns and many grains of the size of about 200 nm are evident in the sample.

B. Critical current density and electrical connectivity

Figure 3(a) shows the $J_c(B)$ curves at 20 K of the analyzed samples obtained from the $M(B)$ curves as[7]

$$J_c=\frac{\Delta M}{(d/2)(1-d/3w)}, \tag{1}$$

where ΔM is the width of the hysteresis loop and d and w $(d\leqslant w)$ are the dimensions of the samples perpendicular to the applied field. The choice of 20 K is taken because of its technological importance.

Among the HIP and RS samples, the highest J_c at low fields, $J_c^{B\to0}$, is observed for samples B1, B2, and B3, with

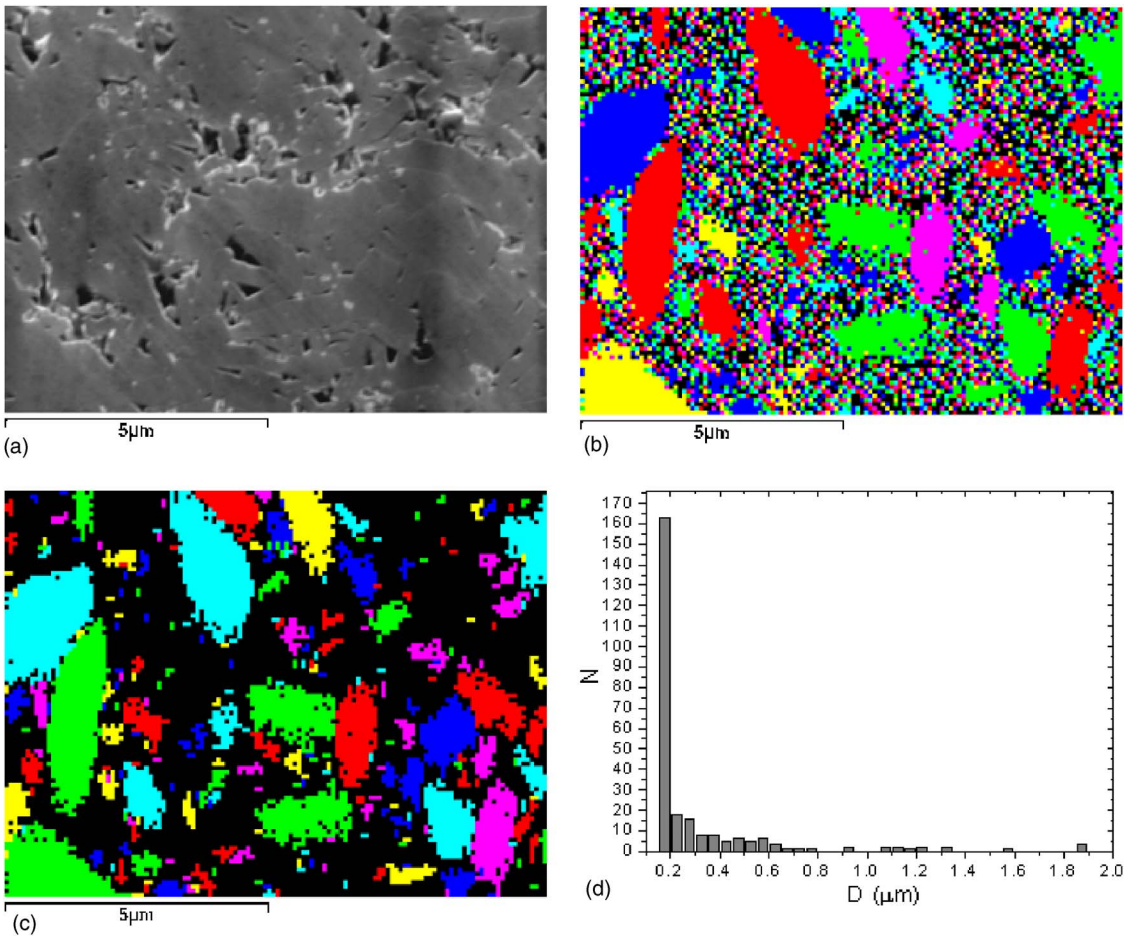

FIG. 1. (Color online) (a) SEM image of sample B3 and (b) its corresponding EBSD map, as measured. (c) The same EBSD map as in (b) after removing single isolated pixels, as explained in the text. (d) Grain-size distribution obtained from (c).

similar values although different magnetic-field decays; the lowest is observed for samples B4 and B5. High $J_c^{B\to 0}$ values are accompanied by low $\Delta\rho$ (Table I), which indicates better grain connectivity of samples B1, B2, and B3 compared with that of samples B4 and B5.[8,9] The SEM microstructure analysis of these samples suggests that poor connectivity is due to accumulation of MgO in the grain boundaries. It should be noted that $\Delta\rho$ for samples B1 and B3 is of the order of that of a fully connected sample ($\Delta\rho_{\text{ideal}} \sim 7.3\ \mu\Omega$ cm).[8,9] For the SiC-doped sample, the increase of resistivity would be associated with the enhancement of electron scattering, consistent with the decrease of RRR, the rise of the upper critical field,[10] and the increase of J_c values at high magnetic fields observed in both bulk B-SiC sample and PIT W-SiC wire. The higher value of $\Delta\rho$ in B-SiC compared with B1 and B3 together with the lower J_c in low fields would indicate worse grain connectivity due to the presence of nonsuperconducting phases. Nevertheless, the high J_c values in high fields indicate underlying powerful pinning mechanisms.

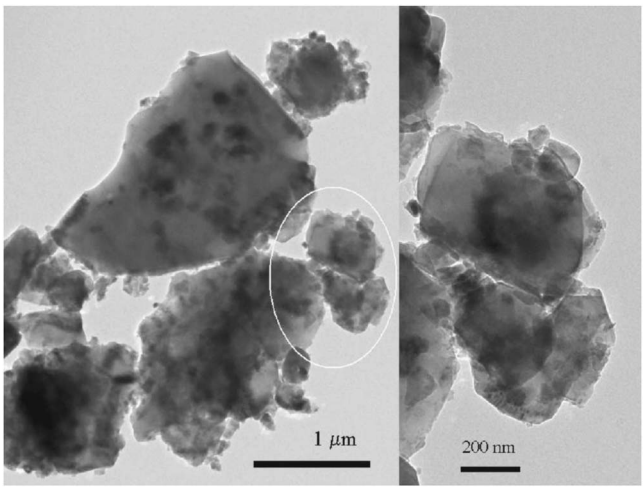

FIG. 2. TEM image of the crushed sample B3.

Figure 3(b) shows the field dependence of the n values characterizing the E-J curves, $E \propto J^n$, for the RS and HIP samples at 20 K, obtained from relaxation experiments as[11]

$$n = 1 + S^{-1} = 1 + \left[-\frac{d\ln(M_{\text{irr}})}{d\ln t} \right]^{-1}, \qquad (2)$$

where $M_{\text{irr}} = \Delta M/2$ is the irreversible magnetization and S is the normalized relaxation rate. The good correlation between the $n(B)$ and $J_c(B)$ curves at high fields suggests that the main limitation to J_c in high fields would be due to flux-

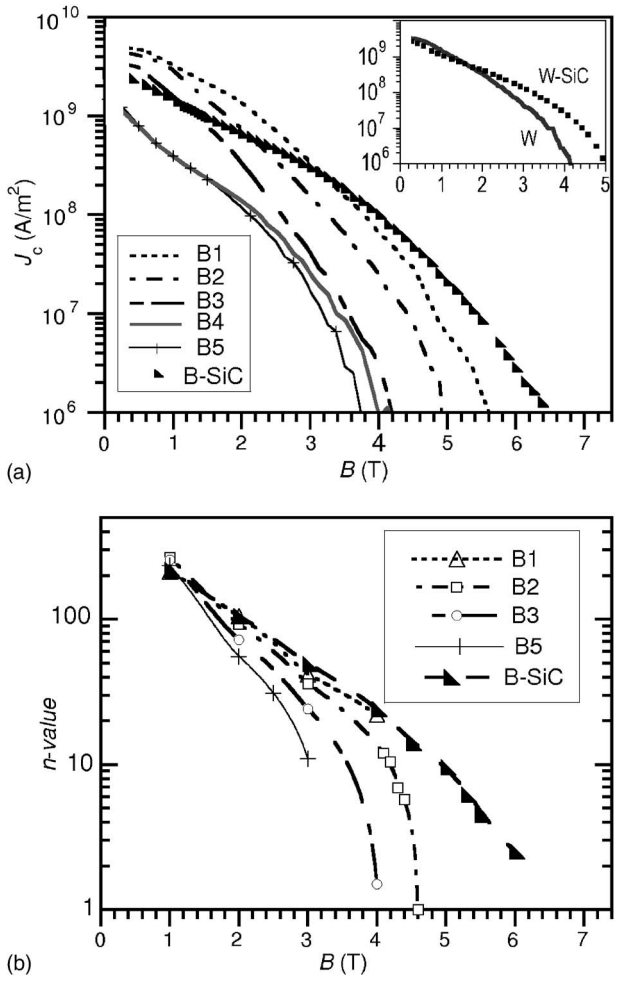

FIG. 3. (a) $J_c(B)$ obtained from magnetization hysteresis loops and (b) $n(B)$ curves calculated from the relaxation experiments at 20 K using Eq. (2).

creep effects. On the contrary, in low magnetic fields most of the samples show similar n values independent of their different J_c. This would be in agreement with the above hypothesis that J_c in low fields is mainly determined by the grain connectivity.

C. Flux pinning curves

In order to compare the behavior of the samples, we have plotted the reduced flux pinning force ($f_p=F_p/F_{p,\max}$) at 20 K as a function of the reduced field $b=B/B^*$ obtained for the SiC-doped samples [Fig. 4(a)] and all undoped samples [Fig. 4(b)], since a particular flux pinning force scaling law is characteristic of a specific pinning mechanism. The value of B^* is the field at which $J_c \to 0$, and therefore, it would be related to the irreversibility field. Flux-creep effects in MgB_2 are important at small J_c [Fig. 3(b)] and, therefore, the irreversibility field will vary depending on the specific criterion used for its estimation or on the time scale of the measurement. In our case, B^* values have been obtained by linear extrapolation to zero of the low-J_c segment of the Kramer curves, $J_c^{1/2}B^{1/4}(B)$, disregarding the zone strongly affected by creep phenomena [discontinuous lines in Figs. 4(c) and 4(d)].

Although the peak of the f_p curves takes place at $b_{\text{peak}} \sim 0.18-0.23$ in all cases, the pinning curves of both SiC-doped samples and the undoped samples with poor J_c values at low magnetic fields (B4 and B5) are well-reproduced by the function $b^{0.5}(1-b)^2$, whereas those of the undoped samples with high $J_c^{B\to 0}$ values (samples B1, B2, B3, and W) are narrower and better described by the function $b^p(1-b)^q$ with higher value of the parameter $q \sim 4$, as seen in the inset of Fig. 4(b). Accordingly, the Kramer plots, commonly used to analyze the pinning mechanisms, are linear for samples B4, B5, and B-SiC with $f_p \propto b^{0.5}(1-b)^2$ [see Fig. 4(c) corresponding to sample B-SiC], but not for samples B1, B2, B3, and W. The results obtained at different temperatures for sample B2 are shown in Fig. 4(d).

In order to clarify the effect of flux creep on the pinning curves, we analyzed the $J_c^{1/2}B^{1/4}$ values obtained at different times of 5 (×) and 60 min (●) after setting the magnetic field. These are plotted in Figs. 4(c) and 4(d). One can see that the curvature of the Kramer curves at the highest fields, when approaching the irreversibility field, is clearly dominated by the flux-creep phenomena. For the rest of the curve, the effect of flux creep is not relevant for any sample, hence it would not be the cause of the different $f_p(b)$ curves obtained on these samples. The magnetic relaxation effects in these samples have been analyzed in more detail in Ref. 12.

Figure 5 shows the reduced flux pinning force as a function of the reduced field for one of these samples, B2, at temperatures of 5–30 K. A similar temperature scaling of the flux pinning force, characterized by the overlapping of $f_p(b)$ curves in the temperature range of 5–30 K, is observed in all analyzed samples. It must be noted that small differences in the value of $b_{\max}$ are expected because of the error in determining B^*.

The peak of the f_p curves takes place at $b_{\text{peak}} \sim 0.2$ for all samples, which seems to be intrinsic to bulk MgB_2. This position of the peak has been observed in MgB_2 in many other works[13–17] and also in some LTSs, such as the A-15 Nb_3Sn (Refs. 18–20) and the Chevrel-phase $PbMo_6S_8$,[21] characterized by $F_p \propto b^{1/2}(1-b)^2$. The quadratic decrease of $F_p \propto (1-b)^2$ at high fields and the position of the peak at $b \sim 0.2$ are characteristic of a pinning mechanism governed by the "flux-line shear mechanism." In this case, the vortices will start to move when the Lorentz force exceeds the flow stress of the flux-line lattice (FLL) and, therefore, F_p is determined by the elastic properties of the flux-line lattice, i.e., $F_p \propto c_{66}$,[5,22–25] where c_{66} is the shear modulus of the FLL.

Nevertheless, as discussed above, in our case the dependence $F_p \propto b^{1/2}(1-b)^2$ [gray thick line in Figs. 4(a) and 4(b)] is only observed for some of the samples. These include both SiC-doped samples and the undoped samples that show low J_c in zero field (samples B4 and B5), whereas $f_p(b)$ curves of most undoped samples are narrower and better described by the function $f_p \propto b^p(1-b)^q$ with $p \approx 1.25$ and $q \approx 4$ [continuous line in the inset of Fig. 4(b)]. This behavior has been also observed by other groups in MgB_2,[13,15] Nb_3Sn,[26,27] and NbTi (Ref. 5) and, therefore, may not be considered as material specific, but caused by a distribution of parameters determin-

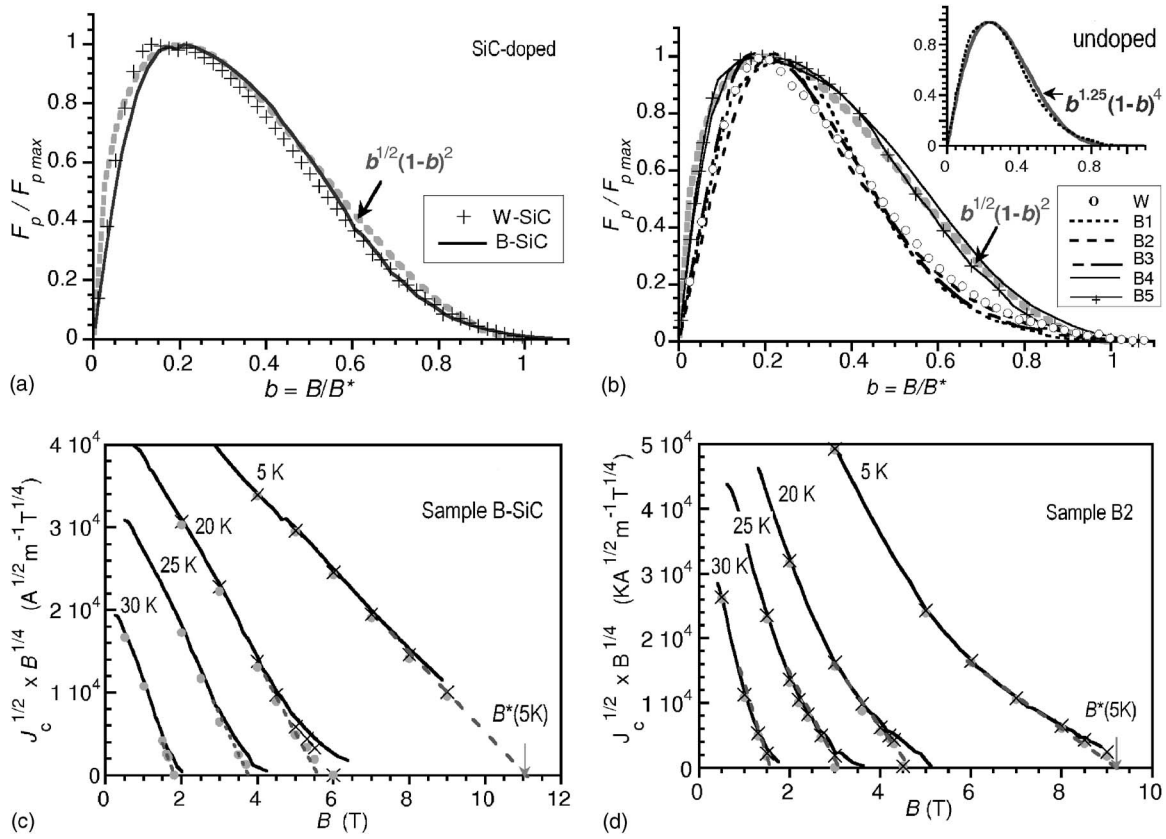

FIG. 4. $f_p(b)$ curves obtained at 20 K for (a) SiC-doped and (b) undoped samples. The gray thick discontinuous line corresponds to the function $b^{1/2}(1-b)^2$ and the continuous line in the inset of (b) represents the function $b^{1.25}(1-b)^4$. (c) and (d) show Kramer plots, $J_c^{1/2}B^{1/4}(B)$ (continuous lines) obtained at different temperatures for samples B-SiC and B2, respectively. The symbols in (b) and (c) correspond to delay times of 5 (×) and 60 (●) min after the set magnetic field is reached. The discontinuous lines are used to estimate $B^*(T)$.

ing F_p combined with the particular choice of B^*. Assuming a Gaussian distribution of the superconducting parameters over the sample, Wördenweber[25] has predicted an increase of parameter q when increasing the width of the distribution.

When changing the temperature, the maximum pinning force increases with B^* and can be fitted by $F_{p,\max} \propto (B^*)^m$. The exponent m ranges from 1.5 to 1.7 for HIP and RS samples, but is higher for PIT samples (≈2.5), although the obtained m values are rough estimates since a limited number of data, corresponding to $T=5$, 20, 25, and 30 K, are available. More measurements would be needed in order to get more accurate m values. The typical value of m for conventional superconductors is ≈2.[20,21] The values of $m = 1.6-2.1$ have also been obtained in MgB_2 superconductor by another group.[14]

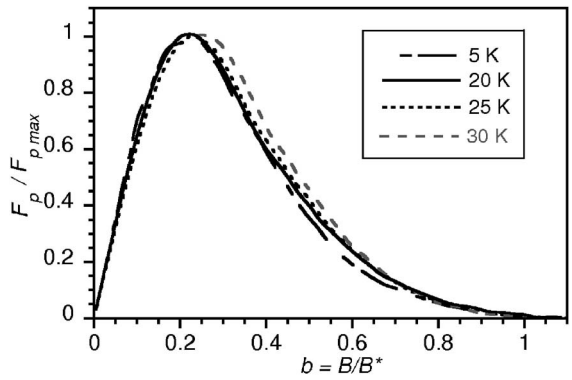

FIG. 5. Reduced flux pinning force ($f_p = F_p/F_{p,\max}$) as a function of the reduced field ($b = B/B^*$) for sample B2 at $T=5$, 20, 25, and 30 K.

The flux-line shear mechanism has been studied in detail and several authors proposed the expressions for F_p based on the flux-lattice shearing. Kramer derived an expression for the pinning force, $F_p \propto b^{1/2}(1-b)^2$, assuming that the flux motion occurs by synchronous shear of the flux lattice around the line pins that are too strong to allow local depinning of the magnetic flux:[22]

$$F_{p\_\mathrm{Kramer}} = \frac{1}{12\pi^2}\frac{1}{a_0(1-a_0/D)^2}c_{66}, \tag{3}$$

where a_0 is the spacing between vortices in a triangular lattice, $a_0 = 1.075(\Phi_0/B)^{0.5}$, $\Phi_0 = 2\times10^{-15}$ T m^{-2} is the flux quantum, and D is the spacing between defects that is normally linked to the grain size of the sample. Using c_{66} as defined by Labush,[28]

$$c_{66} \approx 7.4\times10^4 \frac{B_{c2}^2}{\kappa^2}(1-b)^2, \tag{4}$$

where κ is the Ginzburg-Landau parameter, Kramer obtained the following expression for the flux pinning force:

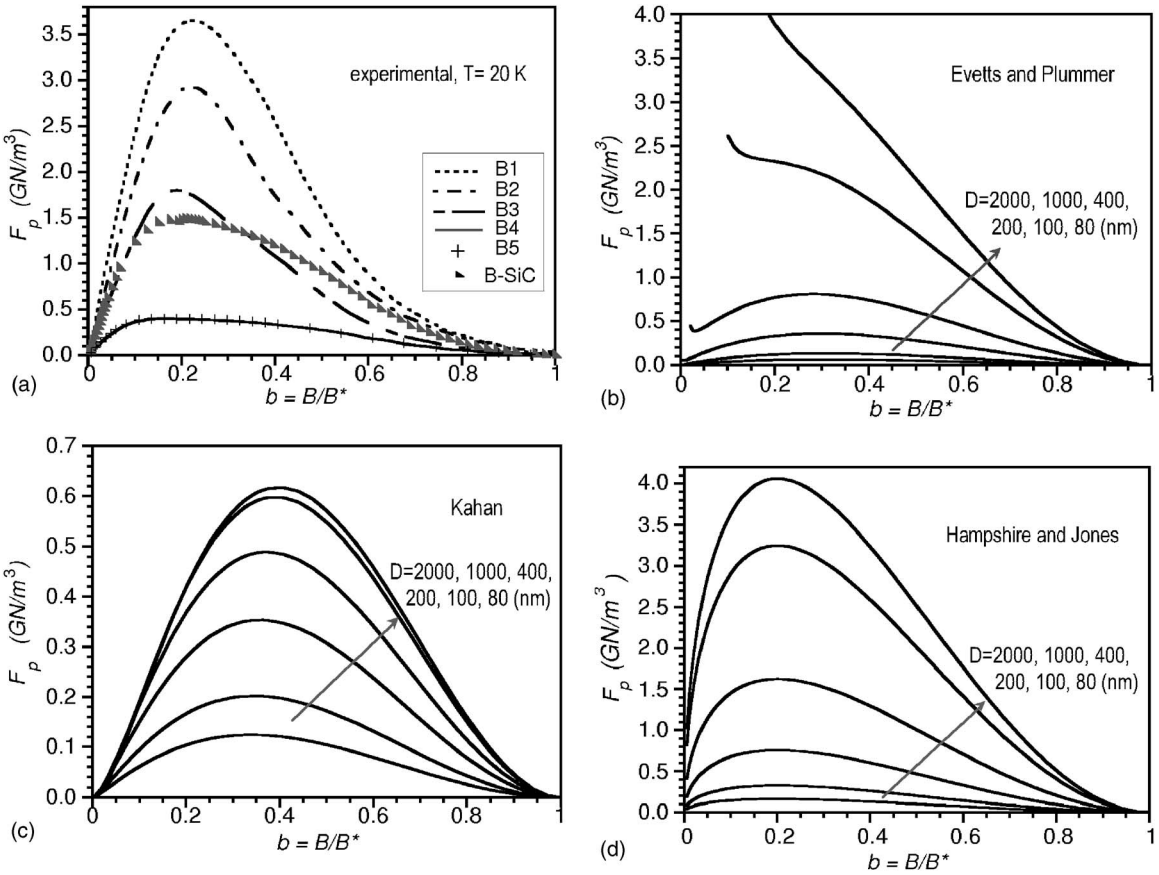

FIG. 6. (a) Experimental $F_p(b)$ curves at 20 K for all measured samples and predictions given by (b) Evetts and Plummer [Eq. (7)], (c) Kahan [Eq. (9)], and (d) Hampshire and Jones [Eq. (10)]. For model calculations, we have used c_{66} given by Eq. (6) and $\kappa=26$ and substitute B_{c2} by $B^*=4.5$ T.

$$F_{p\_\mathrm{Kramer}} = 1.3 \times 10^{10} \frac{1}{(1-a_0/D)^2} \frac{B_{c2}^{5/2}}{\kappa^2} b^{1/2}(1-b)^2. \quad (5)$$

Although the predicted function $F_p \propto b^{1/2}(1-b)^2$ is observed in many superconductors, this formula has two main drawbacks, since it predicts a weak dependence on the grain size, which is in disagreement with experimental observations,[5,18,19] and it uses an expression for c_{66}, which is only valid at high fields, $1-b \ll 1$. If we use a more accurate form for $c_{66}(b)$,[29]

$$c_{66} \approx \frac{B_{c2}^2}{8\mu_0\kappa^2} b(1-b)^2(1-0.58b+0.29b^2), \quad (6)$$

valid at all fields for large κ values ($\kappa \gg 1$), the predicted F_p function is no longer proportional to $b^{1/2}(1-b)^2$.

Subsequent scaling laws, which predict a dependence of F_p on grain size, have been proposed by Evetts and Plummer,[30]

$$F_{p\_\mathrm{EP}} = \frac{1}{\pi} \frac{1}{(D-a_0)} c_{66}, \quad (7)$$

Dew-Hughes,[5]

$$F_{p\_\mathrm{DH}} = \frac{1}{2\pi} \frac{\ln(D/a_0)}{D} c_{66}, \quad (8)$$

which assumes a FLL shear mechanism activated by Frank-Read source dislocations, and Kahan,[24]

$$F_{p\_\mathrm{Kahan}} = \frac{1}{2\pi a_0} \frac{\ln(1+D/a_0)}{(1+D/a_0)} c_{66}, \quad (9)$$

which is very similar to F_{p_DH}, but without the singularity of F_p becoming negative for $D < a_0$. Finally, Hampshire and Jones[23] derived an expression for flux pinning force,

$$F_{p\_\mathrm{HJ}} = \frac{1}{21\mu_0} \frac{1}{D} \frac{B_{c2}^m}{\kappa^s} b^{1/2}(1-b)^2, \quad (10)$$

with the exponents $m=s=2$, also consistent with the grain-boundary pinning mechanism. This expression [Eq. (10)] explained well the pinning behavior in $PbMo_6S_8$ (Ref. 21) and Nb_3Sn (Refs. 18, 19, and 23) with $D > 100$ nm. For smaller grain size, the experimentally obtained $F_{p,\max}$ in Nb_3Sn tend to be smaller than those given by Eq. (10). On the other hand, the Dew-Hughes and Kahan models are in quantitative agreement with the experimental pinning characteristics in irradiated Nb_3Sn.[24]

In order to compare our experimental results with theoretical predictions, in Fig. 6 we plot experimentally obtained

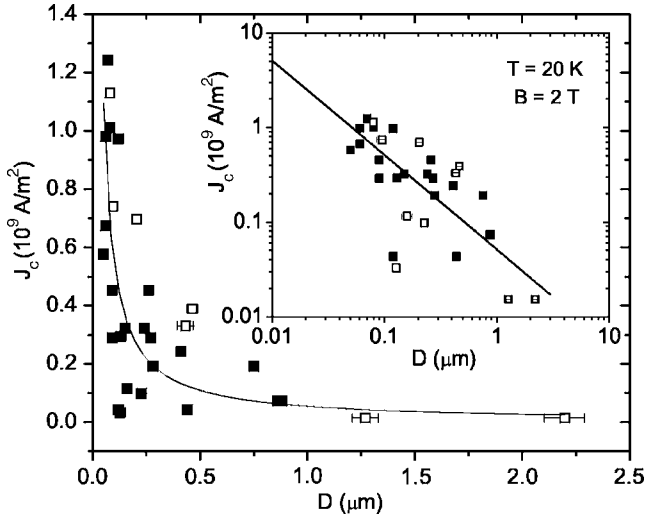

FIG. 7. $J_c(D)$ dependence obtained on 29 dense MgB_2 samples in linear and double logarithmic (inset) scales. The lines are fits to the $1/D$ dependence. The open symbols correspond to undoped samples and the filled symbols to the samples with nanoparticles (SiC, Al_2O_3, TO_2, $SrTiO_3$, $BaTiO_3$, Ni).

$F_p(b)$ at 20 K and the theoretical curves given by Eqs. (7), (9), and (10) for different average grain-size values. We use Eq. (7) to calculate $c_{66}(b)$ and take κ value of 26 obtained in other works for polycrystalline MgB_2.[31–33] The curves in Fig. 6(b)–6(d) were obtained using $B^*=4.5$ T, although B^* varies among the samples in the range between 4.0 and 5.0 T for the undoped samples, and equals 6.2 T for the B-SiC sample. We found that the expressions proposed by Dew-Hughes and Kahan [Fig. 6(c)] reproduce neither the peak position nor the value of $F_{p,\max}$ found in the experiment. On the contrary, we found qualitative agreement between the experimental values of $F_{p,\max}$ and those predicted by Hampshire and Jones for all samples except B5 [Fig. 6(d)]. The function F_{p_EP} also predicts the grain dependence of pinning force similar to the Hampshire and Jones model, although for the smallest D values considered here ($D \leqslant 200$ nm), a singularity is found at $b<0.05-0.25$, when $D<a_0$. Our other finding is that for the samples with poor grain connectivity, the maximum pinning force is low and independent of the grain size and B^*. This could be an artifact of the analysis due to the dominance of the factors other than pinning force. On the contrary, for the samples with good grain connectivity, $F_{p,\max}$ increases with the decrease of the grain size and demonstrates the values similar to the predictions of Hampshire and Jones. This trend is also observed in Fig. 7, which shows J_c value at $B=2$ T and $T=20$ K for several bulk samples, undoped and doped with different nanoparticles. Although with a considerable scattering, the dependence J_c vs $1/D$ is clearly seen in this plot. Possible reasons for the scattering would be the poor grain connectivity in some samples, the error in the estimation of D, and the different scales used to determine J_c and D, as magnetic measurements analyze larger volume of material than EBSD.

The temperature dependence of B^* used in the scaling of $F_p(B)$ curves is shown in Fig. 8 for some of the analyzed samples. The temperature was scaled by $T_c=37.5-38$ K for undoped samples and 35.5 K for the B-SiC sample. The irreversibility field of B-SiC sample obtained from resistivity measurements, $\rho(T,B)$, frequently used to determine the irreversibility field of superconductors, is also plotted in order to show the wide range of temperatures and fields with by very low J_c values controlled by flux creep. In the figure, one can see variation of B^* among the undoped samples, which is larger than the typical error in the estimation of B^* (about 10%–15%). The reason for this variation is still unknown. Nevertheless, all the samples have very similar temperature dependence except B-SiC sample, which has considerably higher B^* and dB^*/dT than undoped samples.

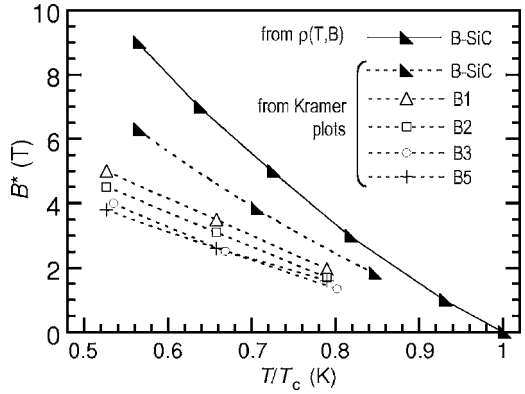

FIG. 8. Temperature dependence of the irreversibility field B^* used in the scaling of $F_p(B)$ curves (symbols with discontinuous lines) for different samples. The irreversibility line obtained for the B-SiC sample from $\rho(T,B)$ measurements, defined as the onset of resistivity, is also shown (symbols with continuous line). The temperature has been scaled by $T_c=37.5-38$ K for undoped samples and 35.5 K for the B-SiC sample.

The J_c in MgB_2 doped with SiC nanoparticles would also be well described by flux-shear models with a parameter B^* higher than in other samples. The pinning is influenced by both extrinsic (density of pinning sites) and intrinsic (κ, B_{c2}) factors. SiC doping produces changes in the intrinsic superconducting characteristics (enhancement of electron scattering, reflected in the decrease of RRR and increase of the upper critical field), which result in the increase of $B^*(T)$ and, therefore, J_c at high fields. On the order hand, our preliminary analysis indicates that the SiC-doped sample has a higher value of the Ginzburg-Landau parameter κ than the undoped ones. This is expected due to diffusion of carbon into MgB_2 and is in agreement with recently published results on carbon-doped samples.[34] According to the above formalism, $F_p \propto \kappa^{-2}$, this will cause a decrease in $F_{p,\max}$, in agreement with the experimental results. The superconducting properties of these doped samples could be further enhanced by improving grain connectivity, which would also result in an increase of $F_{p,\max}$ and J_c in low fields.

IV. CONCLUSION

We have analyzed the effects of grain size, flux creep, and grain connectivity on critical current and pinning properties of bulk MgB_2 materials obtained by RS, HIP, and PIT meth-

ods. We have found that samples with high J_c at low fields also have low $\Delta\rho$ values (Table I), both indicating better grain connectivity comparable to low-J_c samples. The peak of the scaled flux pinning force curves $f_p(b)$, well-described by the function $b^p(1-b)^q$, is situated at about 0.2 for all the samples. The pinning curves of SiC-doped samples and undoped samples with reduced electrical connectivity are well-reproduced by the function $b^{0.5}(1-b)^2$, whereas those of the undoped samples with good grain connectivity are narrower and better described by a higher value of parameter $q \sim 4$. The reason for this difference is still not clear. Moreover, it has been observed that the flux-creep effects do not affect significantly the shape of $f_p(b)$ curves, except when approaching the irreversibility field.

The behavior of MgB_2 samples is reasonably well-described by a traditional flux-shear mechanism of flux pinning with the density of pinning centers mainly determined by the grain size in the bulk. We have observed that for the samples with good grain connectivity, $F_{p,\max}$ increases with the decrease of grain size and has values similar to the predictions for grain-boundary pinning mechanism by Hampshire and Jones [Eq. (10)]. For the samples with reduced grain connectivity, the maximum pinning force is low, independent of their grain size and B^*. More samples are to be investigated for a better understanding of the behavior of MgB_2.

ACKNOWLEDGMENTS

This work was supported by the EU FP6 Project No. NMP3-CT2004-505724 and by the Spanish Ministry of Education and Science, MAT2005-06279-C03-01.

*Corresponding author. Electronic address: elenamar@unizar.es
†Present address: Department of Materials Science and Metallurgy, University of Cambridge, Pembroke Street, Cambridge CB2 3QZ, United Kingdom.

[1] J. Nagamatsu, N. Nakagawa, T. Murakanaka, Y. Zenitani, and J. Akimitsu, Nature (London) **410**, 63 (2001).
[2] S. X. Dou, S. Soltanian, J. Horvat, X. L. Wang, S. H. Zhou, M. Ionescu, H. K Liu, P. Munroe, and M. Tomsic, Appl. Phys. Lett. **81**, 3419 (2002).
[3] H. Yamada, M. Hirakawa, H. Kumakura, A. Matsumoto, and H. Kitaguchi, Appl. Phys. Lett. **84**, 1728 (2004).
[4] W. A. Fietz and W. W. Webb, Phys. Rev. **178**, 657 (1969).
[5] D. Dew-Hughes, Philos. Mag. B **55**, 459 (1987).
[6] E. Martínez, A. Millán, and R. Navarro, Inst. Phys. Conf. Ser. **181**, 2502 (2003).
[7] D. X. Chen, A. Sánchez, J. Nogues, and J. S. Muñoz, Phys. Rev. B **41**, 9510 (1990).
[8] J. Jiang, B. J. Senkowicz, D. C. Larbalestier, and E. E. Hellstrom, Supercond. Sci. Technol. **19**, L33 (2006).
[9] J. M. Rowell, Supercond. Sci. Technol. **16**, R17 (2003).
[10] E. Martínez and R. Navarro, Appl. Phys. Lett. **85**, 1383 (2004).
[11] A. D. Caplin, Y. Bugoslavsky, L. F. Cohen, and G. K. Perkins, Physica C **401**, 1 (2004).
[12] E. Martínez, M. Martínez-López, A. Millán, P. Mikheenko, A. Bevan, and J. S. Abell, presented at the Applied Superconducting Conference, ASC 2006 [IEEE Trans. Appl. Supercond. (to be published)].
[13] S. Keshavarzi, M. J. Qin, S. Soltanian, H. K. Liu, and S. X. Dou, Physica C **408-410**, 601 (2004).
[14] K. Yamamoto, K. Osamura, S. Balamurugan, T. Nakamura, T. Hoshino, and I. Muta, Supercond. Sci. Technol. **16**, 1052 (2003).
[15] D. A. Cardwell, N. Hari Babu, M. Kambara, and A. M. Campbell, Physica C **372-376**, 1262 (2002).
[16] D. C. Larbalestier *et al.*, Nature (London) **410**, 186 (2001).
[17] J. Y. Xiang, D. N. Zheng, J. Q. Li, S. L. Li, H. H. Wen, and Z. X. Zhao, Physica C **386**, 611 (2003).
[18] W. Schauer and W. Schelb, IEEE Trans. Magn. **MAG-17**, 374 (1981).
[19] B. J. Shaw, J. Appl. Phys. **47**, 2143 (1976).
[20] L. D. Cooley, C. M. Fisher, P. J. Lee, and D. C. Larbalestier, J. Appl. Phys. **96**, 2122 (2004).
[21] H. J. Niu and D. P. Hampshire, Phys. Rev. B **69**, 174503 (2004).
[22] E. J. Kramer, J. Appl. Phys. **44**, 1360 (1973).
[23] D. P. Hampshire and H. Jones, J. Phys. C **21**, 419 (1987).
[24] A. Kahan, Phys. Rev. B **43**, 2678 (1991).
[25] R. Wördenweber, Phys. Rev. B **46**, 3076 (1992).
[26] N. Cheggour and D. P. Hampshire, Cryogenics **42**, 299 (2002).
[27] D. M. Kroeger, D. S. Easton, A. DasGupta, C. C. Koch, and J. O. Scarbrough, J. Appl. Phys. **51**, 2184 (1980).
[28] R. Labush, Phys. Status Solidi **32**, 439 (1969).
[29] E. H. Brandt, Phys. Rev. B **34**, 6514 (1986).
[30] J. E. Evetts and C. J. G. Plummer, in *Proceedings of the International Symposium on Flux Pinning and Electromagnetic Properties in Superconductors*, edited by T. Matsushita, K. Yamafuji, and F. Irie (Fukuoka, Matsukuma, 1985), pp. 146–151.
[31] A. G. Joshi, C. G. S. Pillai, P. Raj, and S. K. Malik, Solid State Commun. **118**, 445 (2001).
[32] D. K. Finnemore, J. E. Ostenson, S. L. Bud'ko, G. Lapertot, and P. C. Canfield, Phys. Rev. Lett. **86**, 2420 (2001).
[33] M. Fukuda, E. S. Otabe, and T. Matsushita, Physica C **378-381**, 239 (2002).
[34] C. Krutzler, M. Zehetmayer, M. Eisterer, H. W. Weber, N. D. Zhigadlo, J. Karpinski, and A. Wisniewski, Phys. Rev. B **74**, 144511 (2006).